A Hammerstein Model of the Hand for Precise Control of Electrode Arrays ⋆

Lucy Hodgins * **Chris T. Freeman** * **Zehor Belkhatir** *

* *School of Electronics and Computer Science, University of Southampton, Southampton, UK, SO16 7BT (e-mail: {L.Hodgins,ctf1,Z.Belkhatir}@ soton.ac.uk).*

Abstract: Stroke is a leading cause of disability worldwide, and current interventions are falling short, particularly regarding fine motor movement. Assistive technologies such as functional electrical stimulation offer a promising solution, but require effective control design. Difficulties in obtaining large quantities of data motivate model-based control, however there currently exist no models of the hand suitable for control design. This paper addresses this by deriving a novel Hammerstein model of the hand and wrist. This is validated on experimental data, resulting in 13% error reduction compared to existing models, with far less computational load. The proposed model is suitable for a wide range of control frameworks, facilitating transparent design, constraint handling, and robustness analysis.

Keywords: Model Identification, Functional Electrical Stimulation, Rehabilitation

1. INTRODUCTION

Stroke is one of the leading causes of disability globally, affecting around 100 million people (Feigin et al., 2025). A common consequence of stroke is loss of hand and wrist movement, often leading to a significant reduction in quality of life. This is particularly true for fine dextrous movement, with 62% of those with significant impairment failing to regain this after 6 months (Kwakkel et al., 2003).

Assistive technologies have shown significant benefit, both for orthotic assistance and rehabilitation. The most commonly used is functional electrical stimulation (FES), in which surface electrodes stimulate nerves to artificially contract the underlying muscles. However, accurate control is challenging, particularly for the hand and wrist, due to the complex muscle-tendon network governing the response. Electrode arrays offer a promising solution, however current approaches rely on repeated identification of a linearised system model (Sun and Freeman, 2024), a time-consuming process that limits their wide-spread use.

A key challenge in current FES control design is the lack of a simple but sufficiently accurate model of the hand and wrist. FES control of single joints has benefited from Hammerstein and Hill-type models of muscle dynamics, which can be easily identified (Le et al., 2010) and used to design a wide range of successful controllers without the need for lengthy data-collection procedures. However, no equivalent justified form exists for the multi-input-multi-output (MIMO) structure of the hand and wrist.

The musculoskeletal models that do exist are instead very complex, with a large parameter space that makes their use in control design infeasible. They are largely constructed for the purpose of simulation (McFarland et al., 2023), often requiring access to electromyography data (Crouch and Huang, 2016) or modelling force production rather than precise movement (Paclet and Quaine, 2012).

One exception is the dynamic model proposed in Soska et al. (2012), which accounts for both FES-induced muscle dynamics and the complex tendon coupling between joints. Whilst this model structure has been used to implement iterative learning control (ILC) and model predictive control (MPC) in simulation (Karak et al., 2024), it retains the disadvantage of having an infeasibly large number of parameters for real-world applications. Works such as Hodgins et al. (2024) aim to overcome this by using a multiple-model framework, however the high computational requirements limit the scalability of this approach.

The current paper overcomes these drawbacks by deriving a novel MIMO Hammerstein model of the hand and wrist response to array-based FES stimulation. This model is scalable and is sufficiently flexible to capture the functional complexities of human movement. A feasible approach to parameter identification is presented, enabling the model to be easily implemented in practical control design. This is in contrast to existing model structures, which are shown to be time-consuming and difficult to identify.

The validity of the proposed model is demonstrated using experimental data from eight participants, revealing improved modelling performance compared to the best existing approach, with far less computational time. The proposed model is applicable to a wide range of control frameworks, opening the door to improved controller design and enhanced patient outcomes.

The structure of this paper is as follows. Section 2 introduces the existing models of the hand and wrist, before a simplified Hammerstein form is derived in Section 3. Section 4 presents a transparent identification procedure,

⋆ This work was supported by the U.K. Engineering and Physical Sciences Research Council

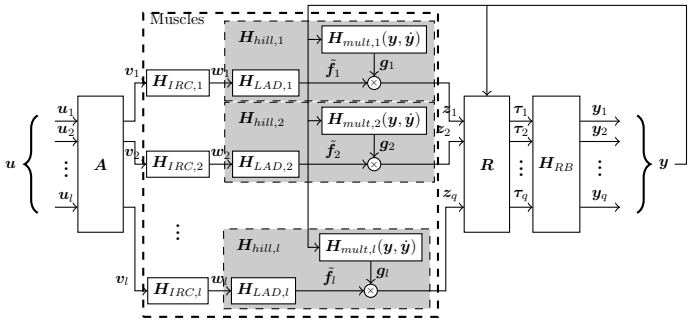

Fig. 1. Block diagram of the hand and wrist model (12)

before the model is experimentally validated in Section 5. Conclusions and future work are given in Section 6.

Notation: Throughout this paper $\mathbb{R}_+$ denotes the set of strictly positive real numbers, $\mathbb{R}^n$ the n-dimensional vector space of real numbers, and $\mathbb{N} = \{0, 1, \dots\}$ the set of natural numbers. $\|\cdot\|$ denotes the 2-norm. Signals and operators are denoted in bold to differentiate them from vectors and functions. For a signal $\boldsymbol{x}$, $\boldsymbol{x}_i$ denotes the i^{th} element, and for a mapping $\boldsymbol{f} : \boldsymbol{x} \mapsto \boldsymbol{y}$, $\boldsymbol{f}_i : \boldsymbol{x}_i \mapsto \boldsymbol{y}_i$. $\mathcal{L}$ denotes the Laplace transform. An n-element signal is in $L_2^n(\mathbb{R}_+)$ if it has bounded energy. $X_{i,j}$ denotes the (i,j)th element of matrix X, and $\text{vec}(X)$ the vertical concatenation. I_n denotes the $n \times n$ identity matrix.

2. PRELIMINARIES

FES electrode arrays are comprised of m separate electrodes pads, arranged in a fixed pattern. An FES sequence $\boldsymbol{u} \in L_2^n(\mathbb{R}_+)$, $n \leq m$ is applied to all or a subset of these electrodes over time instances $t = 0, 1, 2, ...$, inducing movement in joint angles $\boldsymbol{y} \in L_2^q(\mathbb{R}_+)$.

2.1 Existing Hand and Wrist Models

This section introduces the leading existing model structure of the hand and wrist response to FES, which will be used to derive a simplified form in Section 3.

The full mapping $\boldsymbol{u} \mapsto \boldsymbol{y}$ between the applied stimulation and the resulting joint output can be broken down into four components: the electrode array $\boldsymbol{A}$, the muscle response, the tendon network $\boldsymbol{R}$, and the rigid-body dynamics $\boldsymbol{H}_{RB}$, as shown in Figure 1. Each component will now be discussed in detail.

The electrode array is represented by a linear mapping

$$\boldsymbol{A} : L_2^n(\mathbb{R}_+) \to L_2^l(\mathbb{R}_+) : \boldsymbol{u} \mapsto \boldsymbol{v} : v(t) = Au(t) \quad (1)$$

where $\boldsymbol{v}$ gives the stimulation experienced by the l underlying muscle units (Hodgins et al., 2024). The activation of these muscles, $\boldsymbol{w} \in L_2^l(\mathbb{R}_+)$, is determined by an isometric recruitment curve (IRC) , denoted

$$\begin{aligned}\boldsymbol{H}_{IRC} : L_2^l(\mathbb{R}_+) \to L_2^l(\mathbb{R}_+) : \boldsymbol{v} \mapsto \boldsymbol{w} \\ : w_i(t) = H_{IRC,i}(v_i(t))\end{aligned} \quad (2)$$

The function $H_{IRC,i}(\cdot)$ takes a sigmoid shape, with a common approach being to use the form

$$w_i(t) = \alpha_i \frac{e^{\beta_i v_i(t)} - 1}{e^{\beta_i v_i(t)} + \gamma_i}, \quad (3)$$

with parameters α_i, β_i, $\gamma_i \in \mathbb{R}_+$ characterising the muscle's response (Hodgins et al. (2024)).

The mapping between muscle activation $\boldsymbol{w}$ and the generated force $\boldsymbol{f} \in L_2^l(\mathbb{R}_+)$ can be represented using a Hill-type model form, however the common assumption of isometric muscle contraction allows for significant simplification (Soska et al., 2012). The dynamics then compose a linear component $\boldsymbol{H}_{LAD}$ and multiplicative component $\boldsymbol{H}_{mult}(\boldsymbol{y}, \dot{\boldsymbol{y}})$ that models the force-length/ force-velocity properties of the muscle [1] :

$$\begin{aligned}\boldsymbol{H}_{mult} : L_2^l(\mathbb{R}_+) \to L_2^l(\mathbb{R}_+) : \boldsymbol{y} \mapsto \boldsymbol{g} \\ : \boldsymbol{g}_i = \boldsymbol{H}_{mult,i}(\boldsymbol{y}, \dot{\boldsymbol{y}})\end{aligned} \quad (4)$$

with $\boldsymbol{H}_{mult,i}(\boldsymbol{y}, \dot{\boldsymbol{y}})$ defined in Crouch and Huang (2016),

$$\begin{aligned}\boldsymbol{H}_{LAD} : L_2^l(\mathbb{R}_+) \to L_2^l(\mathbb{R}_+) : \boldsymbol{w} \mapsto \tilde{\boldsymbol{f}} \\ : \tilde{\boldsymbol{f}}_i = \mathcal{L}^{-1}(\boldsymbol{H}_{LAD,i}(s)) * \boldsymbol{w}_i\end{aligned} \quad (5)$$

where

$$\boldsymbol{H}_{LAD,i}(s) := \frac{\Omega_i^2}{s^2 + 2\Omega_i s + \Omega_i^2} \quad (6)$$

with $\Omega_i \in \mathbb{R}_+$ denoting the natural frequency of the i^{th} muscle. The full muscle dynamics are thus given by

$$\begin{aligned}\boldsymbol{H}_{hill} : L_2^l(\mathbb{R}_+) \times L_2^l(\mathbb{R}_+) \to L_2^l(\mathbb{R}_+) : (\boldsymbol{y}, \boldsymbol{w}) \mapsto \boldsymbol{f} \\ : \boldsymbol{f}_i = \tilde{\boldsymbol{f}}_i \boldsymbol{g}_i.\end{aligned} \quad (7)$$

where $\boldsymbol{g}_i$ and $\tilde{\boldsymbol{f}}_i$ are defined in (4), (**??**).

The tendon network can be modelled by the operator

$$\begin{aligned}\boldsymbol{R} : L_2^l(\mathbb{R}_+) \times L_2^q(\mathbb{R}_+) \to L_2^q(\mathbb{R}_+) : (\boldsymbol{f}, \boldsymbol{y}) \mapsto \boldsymbol{\tau} \\ : \tau(t) = R(y(t))f(t)\end{aligned} \quad (8)$$

where $\boldsymbol{\tau} \in L_2^q(\mathbb{R}_+)$ represents the torque about the joints, and elements of matrix $R(y(t))$ correspond to the derivative of tendon displacement with respect to each joint angle. The most comprehensive approach (Brook et al., 1995) makes use of Landsmeer's models, with elements given by either (9) or (10) depending on the tendon type, in which $r_{i,j}, d_{i,j}, \tilde{d}_{i,j} \in \mathbb{R}$ are constant anatomical length parameters.

$$R_{i,j}(y(t)) = r_{i,j} \quad (9)$$

$$R_{i,j}(y(t)) = d_{i,j} + \tilde{d}_{i,j}\left(\frac{\sin(y_j(t)) - y_j(t)}{2\sin^2(y_j(t))}\right) \quad (10)$$

Finally, the rigid-body dynamics map the torque $\boldsymbol{\tau}$ to the joint angles $\boldsymbol{y}$ according to

$$\begin{aligned}\boldsymbol{H}_{RB} : L_2^q(\mathbb{R}_+) \to L_2^q(\mathbb{R}_+) : \boldsymbol{\tau} \mapsto \boldsymbol{y} \\ : \ddot{y} = M(y)^{-1}(\tau - C(y,\dot{y})\dot{y} - F(y,\dot{y}) - G(y,\dot{y}))\end{aligned} \quad (11)$$

where $M(y)$ is the inertia matrix, $C(y,\dot{y})$ is the Coriolis matrix, and $F(y,y)$ and $G(y,\dot{y})$ model the effects of friction and gravity respectively. Note that the dependence on time t has been suppressed for notational conciseness [2] .

The full model is then given by the mapping

$$\boldsymbol{y} = \boldsymbol{H}_{RB}\boldsymbol{R}\,\boldsymbol{H}_{hill}\,\boldsymbol{H}_{IRC}\boldsymbol{A}\boldsymbol{u} \quad (12)$$

3. MIMO HAMMERSTEIN MODEL DERIVATION

Hammerstein models are widely used in FES control, consisting of a static non-linearity in series with a linear dynamic system. This separation greatly simplifies both identification and control design (Le et al., 2010). The following section details how the model (12) can be simplified

[1] Note that here $\boldsymbol{H}_{mult,i} : \boldsymbol{y} \mapsto \boldsymbol{g}_i$ rather than the convention $\boldsymbol{H}_{mult,i} : \boldsymbol{y}_i \mapsto \boldsymbol{g}_i$ used elsewhere.

[2] This holds throughout when the meaning is clear from context

to a Hammerstein form, with the added benefit of greatly reducing the number of model parameters. Derivation of this model requires the following assumptions:

Assumption 1. Movement is smooth and slow, with dynamics being dominated by stiffness, damping, and inertia.

Assumption 2. The Coriolis matrix $C(y, \dot{y})$ takes the form

$$C(y, \dot{y}) = \dot{y}^\top \bar{C}(y, \dot{y}). \tag{13}$$

Assumption 3. The friction takes a linear form, given by

$$F(y, \dot{y}) = \begin{bmatrix} k_1(y_{0,1} - y_1(t)) + b_1 \dot{y}_1(t) \\ k_2(y_{0,2} - y_2(t)) + b_2 \dot{y}_2(t) \\ \vdots \\ k_q(y_{0,q} - y_q(t)) + b_q \dot{y}_q(t) \end{bmatrix}, \tag{14}$$

with constants $k_i, b_i \in \mathbb{R}_+$, $y_{0,i} \in \mathbb{R}$, $i = 1, \ldots, q$

Assumption 4. The gravitational force about each joint can be approximated as proportional to the joint angle:

$$G(y) = \begin{bmatrix} \eta_1 y_1(t) + \xi_1 \\ \vdots \\ \eta_q y_q(t) + \xi_q \end{bmatrix}, \tag{15}$$

with constants η_i, ξ_i, $i = 1, \ldots, q$

Assumption 5. The tendon mapping $R(y(t))$ can be approximated by a fixed matrix R.

Assumption 6. The natural frequency of each muscle is equal, given by a constant Ω.

Assumption 7. The multiplicative muscle component $\boldsymbol{H}_{mult,i}$ can be approximated by a constant gain ζ_i.

Assumption 1 is standard in FES-assisted tasks (Le et al., 2010), whilst Assumption 2 can be derived from the Lagrange formulation of a three-link joint (Soska et al., 2012). Assumption 3 was proposed in Soska et al. (2012), and models each joint as a spring with zero elongation about angle $y_{0,i}$. Assumption 4 is less restrictive than in many previous works, which assume gravity to be negligible. The linear form (15) is justified if the deviation of joint angles from their operating point is small. Assumption 5 holds automatically for tendons modelled by (9), and is an approximation used in a range of previous works, e.g. An et al. (1983). Assumption 7 is likewise used in a range of previous works, e.g. Kutlu et al. (2017).

Proposition 8. Given Assumptions 1 - 7 and the hand model (12), the following Hammerstein form is obtained

$$\tilde{\boldsymbol{\mathcal{Y}}}(s) = \boldsymbol{H}(s, \Theta)\, D(d)\, \mathcal{L}(\boldsymbol{h}(\boldsymbol{u}, \Phi)) \tag{16}$$

where $\boldsymbol{\mathcal{Y}} := \mathcal{L}(\boldsymbol{y})$, with output $\tilde{y}(t) := r - y(t)$ defining the joint angle relative to the resting position r corresponding to zero input. $\boldsymbol{H}(s, \Theta) : L_2^q(\mathbb{R}_+) \to L_2^q(\mathbb{R}_+)$ is given by

$$\boldsymbol{H}(s, \Theta) = \begin{bmatrix} \tilde{\boldsymbol{H}}(s, \theta_1) & \cdots & 0 \\ \vdots & \ddots & \vdots \\ 0 & \cdots & \tilde{\boldsymbol{H}}(s, \theta_q) \end{bmatrix} \tag{17}$$

$$\tilde{\boldsymbol{H}}(s, \theta_i) = \frac{1}{\frac{\mu_i}{\Omega^2} s^3 + \left(\frac{2\mu_i}{\Omega} + \frac{1}{\Omega^2}\right) s^2 + \left(\mu_i + \frac{2}{\Omega}\right) s + 1} \tag{18}$$

with parameter vectors

$$\Theta = [\Omega, \mu_1, \mu_2, \ldots, \mu_q]^\top \in \mathbb{R}^{q+1}, \tag{19}$$

$$\theta_i = [\Omega, \mu_i]^\top,\ \mu_i := \frac{b_i}{\eta_i - k_i}. \tag{20}$$

$D(d) \in \mathbb{R}^{q \times l}$ is a constant matrix with elements

$$D_{i,j} := \frac{\alpha_j \zeta_j R_{i,j}}{k_i - \eta_i} \tag{21}$$

where we define parameter vector $d = \mathrm{vec}(D) \in \mathbb{R}^{lq}$, and $\boldsymbol{h}(\boldsymbol{u}, \Phi) := \left[\tilde{\boldsymbol{h}}(\boldsymbol{u}, \phi_1), \ldots, \tilde{\boldsymbol{h}}(\boldsymbol{u}, \phi_l)\right]^\top : L_2^n(\mathbb{R}_+) \to L_2^l(\mathbb{R}_+)$ with elements

$$\tilde{h}(u(t), \phi_j) = \frac{e^{\sum_{k=1}^n \delta_{j,k} u_k(t)} - 1}{e^{\sum_{k=1}^n \delta_{j,k} u_k(t)} + \gamma_j} \tag{22}$$

and parameters

$$\Phi = [\phi_1^\top, \phi_2^\top, \ldots, \phi_l^\top]^\top \tag{23}$$

$$\phi_j = [\delta_{j,1},\ \delta_{j,2}, \ldots, \delta_{j,n}, \gamma_j]^\top,\ \delta_{j,k} = \beta_j A_{j,k}. \tag{24}$$

Proof. Assumption 1 corresponds to $\ddot{y}_i \approx 0$, $\dot{y}_i^2 \approx 0$ which, combined with Assumptions 2 - 4 reduces (11) to

$$\begin{bmatrix} \tau_1 \\ \vdots \\ \tau_q \end{bmatrix} = \begin{bmatrix} k_1 y_{0,1} + \xi_1 - (k_1 - \eta_1) y_1 + b_1 \dot{y}_1 \\ \vdots \\ k_q y_{0,q} + \xi_q - (k_q - \eta_q) y_q + b_q \dot{y}_q \end{bmatrix} \tag{25}$$

$$= \begin{bmatrix} (k_1 - \eta_1)\Big(\underbrace{\frac{k_1 y_{0,1} + \xi_1}{k_1 - \eta_1}}_{r_1} - y_1\Big) + b_1 \dot{y}_1 \\ \vdots \\ (k_q - \eta_q)\Big(\underbrace{\frac{k_q y_{0,q} + \xi_q}{k_q - \eta_q}}_{r_q} - y_q\Big) + b_q \dot{y}_q \end{bmatrix} \tag{26}$$

$$= \begin{bmatrix} (k_1 - \eta_1)\tilde{y}_1 - b_1 \dot{\tilde{y}}_1 \\ \vdots \\ (k_q - \eta_q)\tilde{y}_q - b_q \dot{\tilde{y}}_q \end{bmatrix}. \tag{27}$$

Taking the Laplace transform of (27), combining with the tendon network $R(y(t))$ and muscle dynamics (6), and using Assumptions 5-7, the full dynamics become

$$\begin{bmatrix} -b_1 s + (k_1 - \eta_1) & \cdots & 0 \\ \vdots & \ddots & \vdots \\ 0 & \cdots & -b_q s + (k_q - \eta_q) \end{bmatrix} \begin{bmatrix} \tilde{\boldsymbol{\mathcal{Y}}}_1 \\ \vdots \\ \tilde{\boldsymbol{\mathcal{Y}}}_q \end{bmatrix} \tag{28}$$

$$= \frac{\Omega^2}{s^2 + 2\Omega s + \Omega^2} R \begin{bmatrix} \zeta_1 \boldsymbol{\mathcal{W}}_1 \\ \vdots \\ \zeta_l \boldsymbol{\mathcal{W}}_l \end{bmatrix}$$

where $\boldsymbol{\mathcal{W}}_i := \mathcal{L}(\boldsymbol{w}_i)$. Rearrangement leads to

$$\begin{bmatrix} \tilde{\boldsymbol{\mathcal{Y}}}_1 \\ \vdots \\ \tilde{\boldsymbol{\mathcal{Y}}}_q \end{bmatrix} = \boldsymbol{H}(s, \Theta) \begin{bmatrix} \frac{\zeta_1 R_{1,1}}{k_1 - \eta_1} & \cdots & \frac{\zeta_l R_{1,l}}{k_1 - \eta_1} \\ \vdots & \ddots & \vdots \\ \frac{\zeta_1 R_{q,1}}{k_q - \eta_q} & \cdots & \frac{\zeta_l R_{q,l}}{k_q - \eta_q} \end{bmatrix} \begin{bmatrix} \boldsymbol{\mathcal{W}}_1 \\ \vdots \\ \boldsymbol{\mathcal{W}}_l \end{bmatrix}, \tag{29}$$

where $\boldsymbol{H}(s, \Theta)$ is defined in (17)-(18). Substituting the Laplace transform of (3) and factoring out α_i gives

$$\begin{bmatrix} \tilde{\boldsymbol{\mathcal{Y}}}_1 \\ \vdots \\ \tilde{\boldsymbol{\mathcal{Y}}}_q \end{bmatrix} = \boldsymbol{H}(s, \Theta) \begin{bmatrix} D_{1,1} & \cdots & D_{1,l} \\ \vdots & \ddots & \vdots \\ D_{q,1} & \cdots & D_{q,l} \end{bmatrix} \underbrace{\begin{bmatrix} \mathcal{L}(\tilde{\boldsymbol{h}}(\boldsymbol{u}, \phi_1)) \\ \vdots \\ \mathcal{L}(\tilde{\boldsymbol{h}}(\boldsymbol{u}, \phi_l)) \end{bmatrix}}_{\mathcal{L}(\boldsymbol{h}(\boldsymbol{u}, \Phi))} \tag{30}$$

$$= \boldsymbol{H}(s, \Theta) D(d) \mathcal{L}(\boldsymbol{h}(\boldsymbol{u}, \Phi)) \tag{31}$$

with $\tilde{h}(u, \phi_j)$ defined in (22) and $D_{i,j}$ defined in (21).

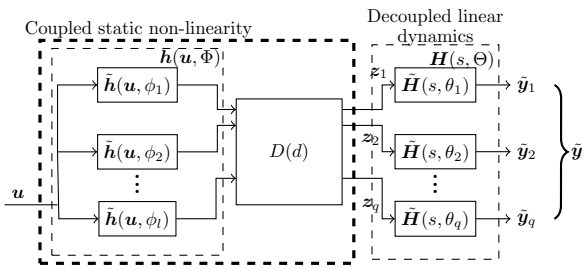

Fig. 2. Hammerstein model structure

Figure 2 shows the proposed model structure. Note that the resting angle r can be easily measured experimentally.

Remark 9. The number of muscles l acts as a hyper-parameter to be selected by the designer. Larger l will give greater model flexibility, at the expense of increased complexity and a risk of over-fitting to small data sets.

4. MODEL IDENTIFICATION

Identification of Hammerstein models has been widely studied in the literature and many possible approaches exist. Given collected input/output data $\{u(t), y(t)\}$, $t = 0, \dots, N$, the objective is to determine parameter vectors $\{\Theta^*, d^*, \Phi^*\}$ that minimise the cost (32), where (33) gives the estimated joint angles.

$$V := \sum_{t=0}^{N} \|y(t) - \hat{y}(t)\|^2 \tag{32}$$

$$\hat{\boldsymbol{y}} = \boldsymbol{r} - \mathcal{L}^{-1}(\boldsymbol{H}(s,\Theta)D(d)\mathcal{L}(\boldsymbol{h}(\boldsymbol{u},\Phi))) \tag{33}$$

One approach well-suited to FES-based identification uses input signals that decouple the static and dynamic responses (Le et al., 2010), allowing each component to be identified separately.

At steady-state the transfer function (17) simplifies to

$$\boldsymbol{H}_{ss}(s,\Theta) := \lim_{s\to 0} \boldsymbol{H}(s,\Theta) = I_q \tag{34}$$

and the time-domain response reduces to

$$\hat{\boldsymbol{y}} = \boldsymbol{r} - D(d)\boldsymbol{h}(\boldsymbol{u},\Phi). \tag{35}$$

Suppose that a set of input-output data $\{u_{ss}, \tilde{y}_{ss}\}$ has been collected at steady-state [3], and assembled into a set $\mathcal{X}$. Then the optimal parameter vectors d^* and Φ^* can be found by solving the following minimisation problem using global non-linear optimisation algorithms:

$$\{d^*, \Phi^*\} = \underset{\substack{d\in\mathbb{R}^{lq}\\ \Phi\in\mathcal{Q}}}{\arg\min} \sum_{\{u,\tilde{y}\}\in\mathcal{X}} \|\tilde{y} - D(d)h(u,\Phi)\| \tag{36}$$

where $\mathcal{Q} := \mathbb{R}_+^{l(n+1)}$.

However, this is difficult to solve using standard methods and lacks parameter interpretability. The following proposition introduces a mapping that transforms (36) into an equivalent form which utilises a more interpretable parameter vector.

Proposition 10. There exists a bijective mapping

$$\mathcal{M} : \mathcal{Q} \to \mathcal{P} : \Phi \mapsto \Psi \tag{37}$$

[3] i.e. $\tilde{y}_{ss} = r - y_{ss}$ where y_{ss} represents the output after input u_{ss} has been applied and the system transients have died out.

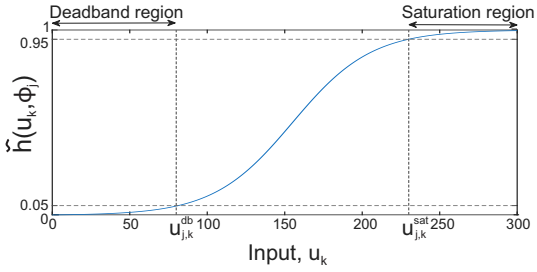

Fig. 3. Example curve of the form (22) for a single input, with deadband and saturation cut-off points given by $u_{j,k}^{\text{db}}$ and $u_{j,k}^{\text{sat}}$ respectively.

defined by

$$\begin{aligned}\mathcal{M}(\Phi) &= [(\tilde{\mathcal{M}}(\phi_1))^\top, (\tilde{\mathcal{M}}(\phi_2))^\top, \dots, (\tilde{\mathcal{M}}(\phi_l))^\top]^\top \\ &= [\psi_1^\top, \psi_2^\top, \dots, \psi_l^\top]^\top = \Psi\end{aligned} \tag{38}$$

$$\tilde{\mathcal{M}}(\phi_j) = \begin{bmatrix} \ln\left((\gamma_j+20)/19\right)/\delta_{j,1} \\ \vdots \\ \ln\left((\gamma_j+20)/19\right)/\delta_{j,n} \\ \ln(19\gamma_j+20)/\delta_{j,1} \end{bmatrix} = \begin{bmatrix} u_{j,1}^{\text{db}} \\ \vdots \\ u_{j,n}^{\text{db}} \\ u_{j,1}^{\text{sat}} \end{bmatrix} = \psi_j \tag{39}$$

where set $\mathcal{P}$ is defined by (40) with $\alpha = 58.404$.

$$\mathcal{P} := \left\{ \Psi \;\middle|\; \begin{array}{c} u_{j,k}^{\text{db}}, u_{j,1}^{\text{sat}} \in \mathbb{R}_+ \\ u_{j,1}^{\text{db}} < u_{j,1}^{\text{sat}} \le \alpha\, u_{j,1}^{\text{db}}, \end{array} \quad j = 1, 2, \dots, l \right\} \tag{40}$$

Proof. For two vectors Φ and $\tilde{\Phi}$, injectivity requires that $\mathcal{M}(\Phi) = \mathcal{M}(\tilde{\Phi}) \implies \Phi = \tilde{\Phi}$. Dividing the last element of (39) by the first yields

$$f(\gamma_j) := \frac{\ln(19\gamma_j + 20)}{\ln\left((\gamma_j+20)/19\right)}, \tag{41}$$

whose monotonicity means that $f(\gamma_j) = f(\tilde{\gamma}_j) \implies \gamma_j = \tilde{\gamma}_j$. From inspection of (39) it's clear this implies $\delta_{j,k} = \tilde{\delta}_{j,k}$, i.e. $\phi_j = \tilde{\phi}_j$ as required. Surjectivity requires showing that $\forall\Psi \in \mathcal{P}$, $\exists\Phi \in \mathcal{Q}$ such that $\mathcal{M}(\Phi) = \Psi$. Function $f(\gamma_j)$ has limits $f(0) = \frac{\ln(20)}{\ln(\frac{20}{19})} = 58.404$, $f(\infty) = 1$, and note that $1 < f(\gamma_j) = u_{j,1}^{\text{sat}}/u_{j,1}^{\text{db}} < 58.404$ leads to (40). The monotonicity of $f(\gamma_j)$ implies for each $j = 1, \dots, l$ a unique solution $\gamma_j \in \mathbb{R}_+$, and corresponding $\delta_{j,k} \in \mathbb{R}_+$ when substituted back into (39). This proves surjectivity and therefore bijectivity. □

Since $\mathcal{M}$ is bijective, the inverse mapping $\mathcal{M}^{-1}$ exists, and thus the solution of (36) corresponds to the solution of

$$\{d^*, \Psi^*\} = \underset{\substack{d\in\mathbb{R}^{lq}\\ \Psi\in\mathcal{P}}}{\arg\min} \sum_{\{u,\tilde{y}\}\in\mathcal{X}} \|\tilde{y} - D(d)h(u,\mathcal{M}^{-1}(\Psi))\| \tag{42}$$

Remark 11. Elements of parameter vector Ψ correspond to the deadband and saturation cut-off points of the non-linear response $\tilde{h}(u_k,\phi_j)$, as shown in Figure 3. In particular $u_{j,k}^{\text{db}}$ and $u_{j,k}^{\text{sat}}$ define the response of the j^{th} muscle to stimulation applied to the k^{th} input. This makes the vector Ψ more interpretable than the original vector Φ, and allows physiological constraints to be easily imposed.

Once the static parameters have been identified, a persistently exciting input $\boldsymbol{u}$ is applied, and we define

$$\hat{\boldsymbol{z}} := D(d^*)\boldsymbol{h}(\boldsymbol{u},\mathcal{M}^{-1}(\Psi^*)). \tag{43}$$

Then the optimal vector Θ^* can be found by using standard gradient-based algorithms to solve the optimisation

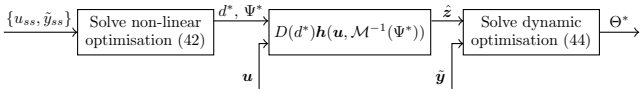

Fig. 4. The proposed 2-step identification algorithm, where u_{ss} and $\tilde{y}_{ss}$ represent steady-state input-output data.

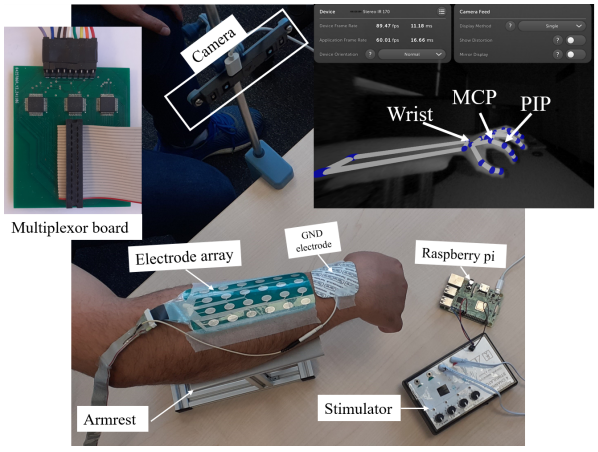

Fig. 5. Hardware used for experimental evaluation.

$$\Theta^* = \underset{\Theta \in \mathbb{R}^{q+1}}{\arg\min} \int_{-\infty}^{\infty} \left\| \tilde{\boldsymbol{\mathcal{Y}}}(s) - \boldsymbol{H}(s, \Theta) \hat{\boldsymbol{\mathcal{Z}}}(s) \right\| ds, \qquad (44)$$

where $\hat{\boldsymbol{\mathcal{Z}}} := \mathcal{L}(\hat{z})$. Figure 4 shows a schematic for the 2-step identification process.

Given optimal parameter values Θ^*, d^* and Ψ^*, the full system model is then given by

$$\hat{\tilde{\boldsymbol{\mathcal{Y}}}}(s) = \boldsymbol{H}(s, \Theta^*) D(d^*) \mathcal{L}\big(\boldsymbol{h}(\boldsymbol{u}, \mathcal{M}^{-1}(\Psi^*))\big). \qquad (45)$$

5. MODEL VALIDATION

The Hammerstein model form (16) will now be validated against experimental data. Code is available at `https://github.com/lgh1g19/IFAC2026`.

5.1 Method

Data were collected from eight unimpaired participants (five male), following ethical approval from University of Southampton (ERGO: FEPS 103765). Code was written in Matlab 2024a and deployed on a Raspberry Pi 3B. This generated 40Hz PWM signals that were amplified by a 4-channel stimulator (Odstock Medical Ltd, Salisbury), then routed through a multiplexor board to a 4×6-element electrode array. These signals were used as the control input $\boldsymbol{u}$, with PWM intensity adjusted between 0-300μs. The hardware is shown in Figure 5.

The voltage levels and the selected array elements were adjusted manually to maximise response and user comfort. A limit was also placed on the maximum combined stimulation level, so that the input space $\mathcal{U}$ was defined by

$$\mathcal{U} := \left\{ u \;\middle|\; \sum_{k=1}^{n} u_k \leq u_{\max}, \quad 0 \leq u_k \leq 300 \right\}, \qquad (46)$$

with values of $u_{\max}$ for each participant given in Table 1.

The identification procedure in Section 4 requires input data that both excites the system dynamics and enables the steady-state response to be observed. This input was

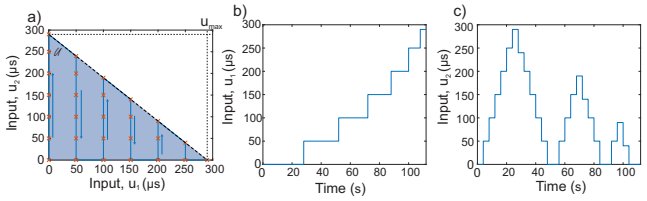

Fig. 6. Input sequence used for model identification, showing direction of traversal through the input space $\mathcal{U}$ (shown in blue). Crosses show the input combinations for which data were collected. Sub-plots b) and c) show corresponding inputs. Data was also collected applying input u_1 as in c) and u_2 as in b).

selected as a series of step inputs of 5s duration, with set $\mathcal{X}$ being constructed from step amplitude u and output y at the end of each step. In order to cover the entire input space, the input sequence shown in Figure 6 was applied. The input space was divided up into 50μs intervals (sub-plot (a)), and the signal $\boldsymbol{u}$ was stepped to each point in turn (sub-plots (b) and (c)). Four sets of data were collected from each participant.

Joint angles $\boldsymbol{y}$ were collected using an UltraLeap Motion Controller 2 camera, before data were processed to remove outliers and camera artifacts. Since existing FES controllers primarily focus on the wrist and index finger (Soska et al., 2012; Karak et al., 2024; Sun and Freeman, 2024), data are presented for the wrist, MCP, and PIP joints only. These joints are shown in Figure 5.

When defining model structure (12), six extrinsic muscles were included, namely the four extensor muscles used in Hodgins et al. (2024), plus the two flexor muscles from Theodorou et al. (2011). The tendon matrix $R(y)$ matched that used in Soska et al. (2012), and the rigid-body dynamics took the forms used in Hodgins et al. (2024). Because the resulting model contained over 70 parameters, sensitivity analysis was used to identify the most influential. These were found to be the array matrix A, joint stiffness k_i, isometric recruitment curve constants β_i and γ_i, and two parameters of matrix $R(y)$, giving a total of 29 parameters. Values were then tuned using global optimisation, however the highly non-linear, dynamic nature of the model made the use of standard tools such as Matlab *GlobalSearch* prohibitively time-consuming. Instead, local gradient-based optimisation was carried out using the interior-point algorithm at multiple randomly-selected start-points.

For the Hammerstein model (16), $l = 2$ was selected to match the number of inputs, yielding a total of 16 parameters. Values were then optimised using the procedure outlined in Section 4. Global optimisation was implemented using the approach described above to ensure fair comparison with model form (12). During the optimisation parameters Ω, d, u^{db}, and u^{sat} were constrained within bounds [0,10], [-150,150], [20,280], [42,600] respectively, to ensure a physiologically relevant solution.

5.2 Results and Discussion

The accuracy of the models (12) and (16) will now be compared. To reduce over-fitting, cross-validation results are presented for each individual. Models were fitted to three of the four collected input-output sets, before being

validated on the final one. This was repeated over all combinations of data, and the mean calculated. Normalised values are given in Table 1 for model (12), and in Table 2 for the Hammerstein model (16). Note that some results have been omitted as the high variability of the collected data made accurate modelling infeasible. This variability also accounts for the high error of the PIP joint.

Table 1 reveals very large normalised error for model (12), whilst Table 2 demonstrates improved fitting (smaller error) in almost all cases. On average the error obtained using the Hammerstein model (16) is 13.2% lower, clearly demonstrating the benefits of the proposed approach.

Table 1. Results for model form (12).

Participant	$u_{\max}$	Normalised error			Time (s)	
		Wrist	MCP	PIP	Mean	Std
1	300	0.860	0.458	-	1820	861
2	220	-	0.598	0.889	1070	656
3	140	0.603	0.534	0.939	352	186
4	150	0.651	0.452	0.542	324	181
5	160	0.563	0.410	-	540	344
6	160	0.595	0.338	0.908	1020	634
7	200	0.241	0.480	0.503	1740	807
8	260	0.667	0.729	0.786	1730	1120
Mean		0.617	0.500	0.744	1019	

Table 2. Results for Hammerstein model (16).

Participant	$u_{\max}$	Normalised error			Time (s)	
		Wrist	MCP	PIP	Mean	Std
1	300	0.659	0.439	-	0.219	0.168
2	220	-	0.478	0.671	0.214	0.223
3	140	0.532	0.564	0.861	0.166	0.146
4	150	0.591	0.427	0.514	0.145	0.116
5	160	0.410	0.399	0.602	0.176	0.132
6	160	0.447	0.322	-	0.186	0.131
7	200	0.299	0.535	0.582	0.118	0.091
8	260	0.559	0.674	0.586	0.198	0.145
Mean		0.499	0.480	0.636	0.178	

Another advantage of the Hammerstein model (16) is the reduced computational requirements. The final columns of Tables 1 and 2 outline the time taken for a single local optimisation step for each model. This reveals that optimisation of the Hammerstein model (16) is four orders of magnitude faster than applying the same approach to the model (12). This difference arises from both the reduced number of parameters and the efficiency of the 2-step optimisation proposed in Section 4.

6. CONCLUSIONS

This paper has presented a novel Hammerstein form of hand and wrist model suitable for model-based control design, along with a practical approach to parameter identification. This model demonstrated a 13% reduction in cross-validation error compared to existing approaches. The proposed model also exhibits significantly reduced computational time, making it far more suitable for integration into practical systems.

Future work will validate the model in a wider range of situations and on a larger participant sample size. The model will also be incorporated into suitable control architectures, enabling simple implementation of optimal control approaches with transparent performance guarantees.

REFERENCES

An, K., Ueba, Y., Chao, E., Cooney, W., and Linscheid, R. (1983). Tendon excursion and moment arm of index finger muscles. *J. Biomech.*, 16(6), 419–425.

Brook, N., Mizrahi, J., Shoham, M., and Dayan, J. (1995). A biomechanical model of index finger dynamics. *Med. Eng. Phys.*, 17(1), 54–63.

Crouch, D.L. and Huang, H. (2016). Lumped-parameter electromyogram-driven musculoskeletal hand model: A potential platform for real-time prosthesis control. *J. Biomech.*, 49(16), 3901–3907.

Feigin, V., Brainin, M., Norrving, B., Martins, S., Pandian, J., Lindsay, P., Grupper, M., and Rautalin, I. (2025). World stroke organization: Global stroke fact sheet 2025. *International Journal of Stroke*, 20(2), 132–144.

Hodgins, L., Freeman, C., and Belkhatir, Z. (2024). Multiple model iterative learning control of FES electrode arrays. *21st international conference on informatics in control, automation and robotics*.

Karak, T., Basak, S., Joseph, P.A., and Sengupta, S. (2024). Non-linear model predictive control based trajectory tracking of hand and wrist motion using functional electrical stimulation. *Control Eng. Pract.*, 146.

Kutlu, M., Freeman, C., Hughes, A.M., and Spraggs, M. (2017). A home-based FES system for upper-limb stroke rehabilitation with iterative learning control. *IFAC-PapersOnLine*, 50(1), 12089–12094. 20th IFAC World Congress.

Kwakkel, G., Kollen, B.J., van der Grond, J., and Prevo, A.J.H. (2003). Probability of regaining dexterity in the flaccid upper limb: impact of severity of paresis and time since onset in acute stroke. *Stroke*, 34 9, 2181–6.

Le, F., Markovsky, I., Freeman, C.T., and Rogers, E. (2010). Identification of electrically stimulated muscle models of stroke patients. *Control Eng. Pract.*, 18, 396–407.

McFarland, D., Binder-Markey, B., Nichols, J., Wohlman, S., Bruin, M., and Murray, W. (2023). A musculoskeletal model of the hand and wrist capable of simulating functional tasks. *IEEE Trans. Biomed. Eng.*, 70(5), 1424–1435.

Paclet, F. and Quaine, F. (2012). Motor control theories improve biomechanical model of the hand for finger pressing tasks. *J. Biomech.*, 45(7), 1246–1251. doi: https://doi.org/10.1016/j.jbiomech.2012.01.038.

Soska, A., Freeman, C., and Rogers, E. (2012). ILC for FES-based stroke rehabilitation of hand and wrist. In *2012 IEEE International Symposium on Intelligent Control (ISIC)*, 1267–1272. IEEE.

Sun, X. and Freeman, C.T. (2024). Parameterised function ILC with application to stroke rehabilitation. *Control Engineering Practice*, 145.

Theodorou, E., Todorov, E., and Valero-Cuevas, F.J. (2011). Neuromuscular stochastic optimal control of a tendon driven index finger model. In *Proceedings of the 2011 American Control Conference*, 348–355. IEEE.